JOURNAL OF AIRCRAFT
Vol. 43, No. 2, March–April 2006

Estimating the Probability of Failure of a Nonlinear Aeroelastic System

Daniel R. Millman*
U.S. Air Force Flight Test Center, Edwards Air Force Base, California 93524
Paul I. King† and Raymond C. Maple‡
Air Force Institute of Technology, Wright–Patterson Air Force Base, Ohio 45433
Philip S. Beran§
U.S. Air Force Research Laboratory, Wright–Patterson Air Force Base, Ohio 45433
and
Lawrence K. Chilton¶
Air Force Institute of Technology, Wright–Patterson Air Force Base, Ohio 45433

A limit-cycle oscillation (LCO) can be characterized by a subcritical or supercritical bifurcation, and bifurcations are shown to be discontinuities in the stochastic domain. The traditional polynomial-chaos-expansion method, which is a stochastic projection method, is too inefficient for estimating the LCO response surface because of the discontinuities associated with bifurcations. The objective of this research is to extend the stochastic projection method to include the construction of B-spline surfaces in the stochastic domain. The multivariate B-spline problem is solved to estimate the LCO response surface. A Monte Carlo simulation (MCS) is performed on this response surface to estimate the probability density function (PDF) of the LCO response. The stochastic projection method via B-splines is applied to the problem of estimating the PDF of a subcritical LCO response of a nonlinear airfoil in inviscid transonic flow. A probability of failure based upon certain failure criteria can then be computed from the estimated PDF. The stochastic algorithm provides a conservative estimate of the probability of failure of this aeroelastic system two orders of magnitude more efficiently than performing an MCS on the governing equations.

Nomenclature

$B_{i,k_{\xi_1},x_{\xi_1}}$	=	ith B-spline of order k_{ξ_1} for the knot sequence $\boldsymbol{x}_{\xi_1}$
$B_{j,k_{\xi_2},x_{\xi_2}}$	=	jth B-spline of order k_{ξ_2} for the knot sequence $\boldsymbol{x}_{\xi_2}$
b	=	airfoil midchord
C_l	=	lift coefficient
C_m	=	moment coefficient about the elastic axis
c	=	airfoil chord
D_h	=	plunge viscous damping constant
D_α	=	pitch viscous damping constant
d	=	dimension of $\boldsymbol{\xi}$
$\boldsymbol{E}, \boldsymbol{F}$	=	flux vectors
E_t	=	total energy
I, J	=	defines the nodes on the ξ_1 and ξ_2 axes, respectively
K_h	=	plunge spring constant
K_α	=	pitch spring constant
k_{ξ_1}, k_{ξ_2}	=	order of the B-splines on the ξ_1 and ξ_2 axes, respectively
m	=	airfoil mass
N	=	number of realizations in a Monte Carlo simulation
P	=	upper limit of a chaos expansion
p	=	pressure
$\boldsymbol{Q}$	=	vector of conserved variables
r_α	=	nondimensional radius of gyration about the elastic axis
t	=	time
U	=	contravarient velocity
u	=	x component of velocity
V	=	velocity, contravariant velocity
V_r	=	reduced velocity
v	=	y component of velocity
$w(\boldsymbol{\xi})$	=	Gaussian distribution
x	=	horizontal coordinate of the grid
x_{cg}	=	nondimensional distance from the airfoil leading edge to the center of gravity of the airfoil
x_α	=	nondimensional distance from the elastic axis to the center of mass of the airfoil
$\boldsymbol{x}_{\xi_1}, \boldsymbol{x}_{\xi_2}$	=	vectors containing the knots on the ξ_1 and ξ_2 axes, respectively
y	=	nondimensional plunge displacement of the elastic axis, vertical coordinate of the grid
α	=	pitch angle
β_α	=	cubic pitch spring constant
γ_α	=	quintic pitch spring constant
ζ_h, ζ_α	=	coefficients of viscous damping for plunge and pitch, respectively
ζ_y	=	plunge-damping coefficient
ζ_α	=	pitch-damping coefficient
μ_s	=	airfoil/air mass ratio
$\boldsymbol{\xi}$	=	vector containing the zero mean, unit variance Gaussian random variables $(\xi_1, \xi_2, \ldots, \xi_d)$
ρ	=	density
Ψ_i	=	ith chaos basis function
ω_h	=	plunge natural frequency
ω_r	=	frequency ratio
ω_α	=	pitch natural frequency

Subscripts

fail	=	failure mode values

Received 13 September 2004; revision received 1 February 2005; accepted for publication 14 February 2005.

*AFIT Adjunct Assistant Professor, Major, USAF, U.S. Air Force Test Pilot School. Senior Member AIAA.
†Professor, Department of Aeronautics and Astronautics. Senior Member AIAA.
‡Assistant Professor, Lt. Col., USAF, Department of Aeronautics and Astronautics. Senior Member AIAA.
§Senior Research Aerospace Engineer, AFRL/VASD. Associate Fellow AIAA.
¶Associate Professor, Department of Mathematics and Statistics.

LCO = limit-cycle oscillation values
∞ = freestream values

Superscripts

$\bar{\ }$ = mean values
$\tilde{\ }$ = standard deviation values
$\hat{\ }$ = coefficients of the chaos expansions

Introduction

FLUID-STRUCTURE interaction can result in the loss of dynamic stability to a time-periodic instability that grows unbounded, that is, flutter.[1] When nonlinear aerodynamics (e.g., transient shocks or boundary-layer separation) or nonlinear structural parameters are present to counter the growth of the unstable mode, the dynamic response can stabilize to a limit-cycle oscillation (LCO).[2] The study of LCO in aeroelastic systems is an active area of research.[3–6] Flight data from fighter aircraft with external stores indicate that the LCO response is characterized by antisymmetric motion of the wing and a lateral motion of the fuselage and, consequently, the aircrew. LCO can lead to fatigue failure of the wing structure. The lateral motion LCO induces can degrade mission effectiveness by not allowing the aircrew to track a target or lead the aircrew to believe that the aircraft has begun to flutter, causing a mission abort. In severe cases, LCO represents a hazard to flight safety.[2]

Computational-fluid-dynamics (CFD) methods have been coupled with structural solvers to provide accurate predictions of LCOs.[7] There is, however, a growing interest in understanding how uncertainties in flight conditions and structural parameters affect the character of an LCO response, leading to failure of an aeroelastic system.[8] Uncertainty quantification of a stochastic system (parametric uncertainty) with stochastic inputs (initial condition uncertainty) has traditionally been analyzed with Monte Carlo simulations (MCS).[9] In an MCS, N random realizations of the uncertainty parameters are input into the system of equations to obtain N realizations of the response. The probability density function (PDF) of the response is then approximated from the N realizations. The MCS method only requires that the distribution of the input parameters be known. A CFD solution, however, can take days to weeks to obtain a single response, making the MCS method intractable for large problems.

Other techniques that have been used to solve stochastic systems with stochastic inputs are based upon Galerkin's method.[9–11] These include reduced-order modeling (ROM)[12–14] and polynomial chaos expansions (PCE).[9,15–23] The reduced-order model represents a full order solution with an optimal basis, in the mean-square sense, through a Karhunen–Loeve expansion. Monte Carlo simulations can efficiently be run on the ROM, but only for small variations in the inputs. Thus, ROM is useful for examining responses near the mean value but cannot predict responses with large variations in the input.[12] The PCE method, on the other hand, allows large variations in the input parameters and has been shown, for certain classes of problems, to be far more efficient than an MCS.[17] The classical PCE method, also known as the Wiener–Hermite expansion,[24] falls into a general category of stochastic projection methods. Of the two methods, ROM or stochastic projection, the stochastic projection method was chosen, because of its greater efficiency and robustness in handling large variations, to quantify the effects of uncertainty and estimate the probability of failure for a nonlinear aeroelastic system.

Stochastic projection methods provide a way to estimate the expansion of a response without a priori knowledge of the form of the response in the stochastic domain. A random basis, denoted $\Psi_i(\boldsymbol{\xi})$, orthogonal with respect to the distribution of the input uncertainty is typically selected. The deterministic coefficients of the expansion $\hat{\alpha}_i(t)$ are either computed as part of the time integration (intrusive approach) or estimated from a limited MCS (nonintrusive approach). The expansion of some response $\alpha(t, \boldsymbol{\xi})$ then takes the form[16,17]

$$\alpha(t, \boldsymbol{\xi}) = \sum_{i=0}^{P} \hat{\alpha}_i(t)\Psi_i(\boldsymbol{\xi}) \tag{1}$$

where the upper limit P is based on the order of the expansion and the number of input uncertainties, that is, the dimension d of $\boldsymbol{\xi}$. The vector $\boldsymbol{\xi}$ contains the random variables that characterize the uncertainty distribution of the input parameters. For a Gaussian distribution, the uncertainty of some input parameter β_α is characterized by its mean value $\bar{\beta}_\alpha$ and its standard deviation $\tilde{\beta}_\alpha$ as

$$\beta_\alpha = \bar{\beta}_\alpha + \xi_1\tilde{\beta}_\alpha \tag{2}$$

where ξ_1 is a zero-mean, unit variance Gaussian random variable.

With the intrusive approach, the expansion in Eq. (1) is substituted directly into the governing equations of motion. For example, consider an equation of motion with the form

$$\mathcal{L}[\alpha(t)] + \beta_\alpha\alpha^3 = 0 \tag{3}$$

where $\mathcal{L}$ is a linear differential operator. Substituting Eqs. (1) and (2) into Eq. (3) yields

$$\mathcal{L}\left[\sum_{i=0}^{P}\hat{\alpha}_i\Psi_i\right] + \bar{\beta}_\alpha\sum_{i=0}^{P}\sum_{j=0}^{P}\sum_{k=0}^{P}\hat{\alpha}_i\hat{\alpha}_j\hat{\alpha}_k\Psi_i\Psi_j\Psi_k + \tilde{\beta}_\alpha\sum_{i=0}^{P}\sum_{j=0}^{P}\sum_{k=0}^{P}\hat{\alpha}_i\hat{\alpha}_j\hat{\alpha}_k\xi_1\Psi_i\Psi_j\Psi_k = 0 \tag{4}$$

To deal with expected values rather than random values, a Galerkin approach is employed. Equation (4) is multiplied by the basis Ψ_n and the Gaussian PDF w, which for d uncertainties is given by

$$w(\boldsymbol{\xi}) = \left(1/\sqrt{2\pi}\right)^d e^{-\frac{1}{2}\xi^T\xi} \tag{5}$$

to obtain

$$\mathcal{L}\left[\sum_{i=0}^{P}\sum_{n=0}^{P}\hat{\alpha}_i\Psi_i\Psi_n w\right] + \bar{\beta}_\alpha\sum_{i=0}^{P}\sum_{j=0}^{P}\sum_{k=0}^{P}\sum_{n=0}^{P}\hat{\alpha}_i\hat{\alpha}_j\hat{\alpha}_k\Psi_i\Psi_j\Psi_k\Psi_n w + \tilde{\beta}_\alpha\sum_{i=0}^{P}\sum_{j=0}^{P}\sum_{k=0}^{P}\sum_{n=0}^{P}\hat{\alpha}_i\hat{\alpha}_j\hat{\alpha}_k\xi_1\Psi_i\Psi_j\Psi_k\Psi_n w = 0 \tag{6}$$

Equation (6) is then integrated over the range of the Gaussian PDF w. The expected value operator for d uncertainty parameters is defined as

$$\langle f(\boldsymbol{\xi}), \Psi_n(\boldsymbol{\xi})\rangle = \int_{-\infty}^{\infty}\int_{-\infty}^{\infty}\cdots\int_{-\infty}^{\infty} f(\boldsymbol{\xi})\Psi_n(\boldsymbol{\xi})w(\boldsymbol{\xi})\,\mathrm{d}\xi_1\,\mathrm{d}\xi_2\cdots\mathrm{d}\xi_d \tag{7}$$

where $f(\boldsymbol{\xi})$ is any function of $\boldsymbol{\xi}$. By application of the expected value operator, Eq. (6) becomes

$$\mathcal{L}\left[\sum_{i=0}^{P}\sum_{n=0}^{P}\hat{\alpha}_i\langle\Psi_i, \Psi_n\rangle\right] + \bar{\beta}_\alpha\sum_{i=0}^{P}\sum_{j=0}^{P}\sum_{k=0}^{P}\hat{\alpha}_i\hat{\alpha}_j\hat{\alpha}_k\langle\Psi_i\Psi_j\Psi_k, \Psi_n\rangle + \tilde{\beta}_\alpha\sum_{i=0}^{P}\sum_{j=0}^{P}\sum_{k=0}^{P}\hat{\alpha}_i\hat{\alpha}_j\hat{\alpha}_k\langle\xi_1\Psi_i\Psi_j\Psi_k, \Psi_n\rangle = 0 \tag{8}$$

Because of the orthogonality of the basis Ψ_n with the Gaussian PDF w, the only terms that survive in the linear differential operator $\mathcal{L}$ are those where $i = n$. Thus the stochastic projection of the equation of motion given in Eq. (3) becomes a system of n equations, which can be written as

$$\mathcal{L}[\hat{\alpha}_n] + \bar{\beta}_\alpha\sum_{i=0}^{P}\sum_{j=0}^{P}\sum_{k=0}^{P}\hat{\alpha}_i\hat{\alpha}_j\hat{\alpha}_k\frac{\langle\Psi_i\Psi_j\Psi_k, \Psi_n\rangle}{\langle\Psi_n, \Psi_n\rangle} + \tilde{\beta}_\alpha\sum_{i=0}^{P}\sum_{j=0}^{P}\sum_{k=0}^{P}\hat{\alpha}_i\hat{\alpha}_j\hat{\alpha}_k\frac{\langle\xi_1\Psi_i\Psi_j\Psi_k, \Psi_n\rangle}{\langle\Psi_n, \Psi_n\rangle} = 0 \tag{9}$$

The condition of orthogonality with respect to the Guassian PDF substantially reduces the number of nonzero expected values for a

linear problem. As nonlinearity increases, the number of nonzero terms grows rapidly because of the coupling evident in Eq. (9). Computational efficiency is rapidly lost when high-order expansions of highly nonlinear equations are required.[24–28]

To gain back some computational efficiency, researchers have employed the nonintrusive approach. This is a sampling approach and considered nonintrusive because parametric uncertainty is not included analytically in the equations of motion. A limited MCS is performed, and the responses obtained are used to estimate the coefficients of the expansion. Because of the random selection of samples, the expected value operator is again employed. The coefficients are estimated from[8]

$$\hat{\alpha}_i = \langle \alpha, \Psi_i \rangle / \langle \Psi_n, \Psi_n \rangle \tag{10}$$

This nonintrusive approach substantially reduces the number of expected values that need to be precomputed and stored and is considered more appropriate for highly nonlinear problems.

Thus far the discussion has centered around the mathematics of the stochastic projection method. The stochastic projection also has a physical interpretation, that is, it can be viewed as approximating the response surface across the entire stochastic domain.[9,17,27] The stochastic projection method, though, differs from traditional response surface methodologies (RSM)[29] in that the expansion is global, whereas RSM is concerned with local expansions about some point of interest. Thus, the stochastic projection method is an interpolation algorithm. This viewpoint explains many of the issues that, in particular, caused the PCE approach to be mostly abandoned by the 1970s.[17] The original PCE method assumed a Gaussian uncertainty in the parameters, and the orthogonal basis functions chosen for the expansion were the Hermite polynomials.[15–17] Chorin[24] discussed the lack of sufficient frequency content in the Hermite polynomials to approximate discontinuities to stochastic solutions of the inviscid Burger's equation. Crow and Canavan[25] demonstrated that, although only low-order Hermite expansions are computationally practical, high-order Hermite polynomials are required to allow an energy cascade for approximating a turbulent flow.

Despite these findings, recent literature on the generalized PCE through an Askey scheme,[21] which matches distribution functions to the appropriate orthogonal polynomials, still cites the optimality of polynomial expansions without regard to the issue of frequency content. Millman et al.,[26,27] however, showed that by changing to a Fourier basis, termed a Fourier chaos expansion (FCE), stochastic projections with discontinuities could be better approximated. A comparison of the stochastic projections from the PCE and FCE approaches is shown in Fig. 1, where for this example the random variable ξ_2 represents the uncertainty in the initial pitch angle of a nonlinear airfoil in the presence of modeled aerodynamics.[27] The ability of the FCE to better approximate the discontinuity than the PCE method leads to a better approximation of the PDF of the LCO response, as shown in Fig. 2. These results are based on the intrusive method, and, although a substantial improvement over the PCE method, the FCE method was still too computationally inefficient to be useful in a design environment due to multiple summations such as the ones in Eq. (9).

Numerical techniques have been advanced to overcome the computational expense of computing the multiple summations. For example, Mathelin and Hussaini[30] employ a stochastic collocation scheme in the PCE solution of the Reimann problem, which reduces the computational effort from order P^3, $\mathcal{O}(P^3)$, to $\mathcal{O}(P)$. However, they note that the upper limit P has to be large ($P = 200$) to accurately account for the moving discontinuity.[30]

It has been shown that bifurcations, such as the LCO response of an airfoil, are discontinuities in the stochastic domain.[27,31] Thus, the numerical issues faced by Chorin,[24] Crow and Canavan,[25] and Mathelin and Hussaini[30] must be dealt with in an efficient manner. In interpolation theory, discontinuities are treated as piecewise polynomials, and researchers commonly employ B-splines to approximate these piecewise polynomials.[32] Constructing B-spline surfaces is also a collocation approach because the nodes of the surface are fitted exactly.[33] The nodes of the response (B-spline) surface can be computed from a nonintrusive approach and, because the B-spline

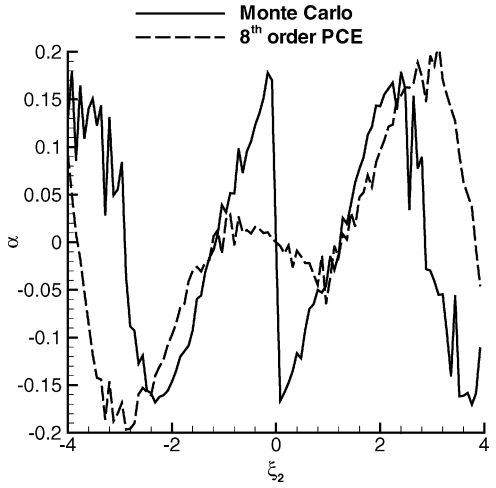

a) MCS vs eighth-order PCE

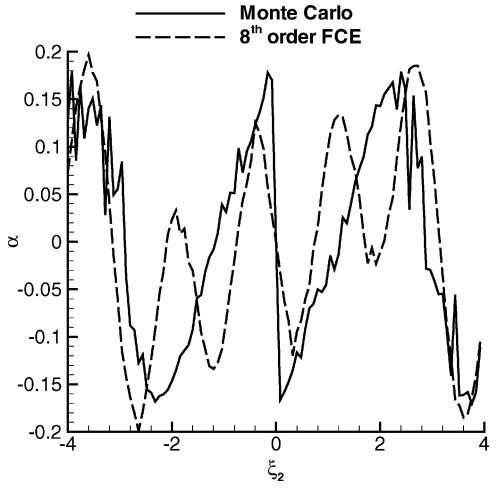

b) MCS vs eighth-order FCE

Fig. 1 $\alpha(t, \xi)$ at $t = 2000$ vs ξ_2 (Ref. 27).

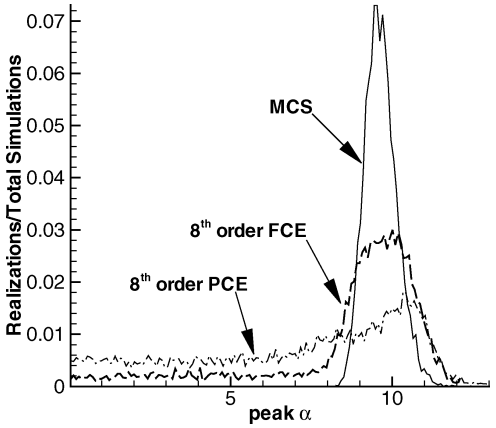

Fig. 2 PDFs of a supercritical response, MCS vs eighth-order PCE and FCE.[27]

method is non-Galerkin, expected values need not be computed or stored.[31]

Stochastic Projection Method via B-Splines

Stochastic projections, that is, the projection of the response onto the stochastic domain, can be treated as piecewise continuous over the interval of interest. Splines would then be an appropriate choice for approximating the stochastic projections. An important property of the multivariate B-splines chosen for this work is that they

are a compact support basis, that is, the influence of any particular B-spline coefficient extends over a few intervals.[33] The practical importance of this property is that oscillations in the vicinity of discontinuous behavior can be avoided with the proper choice in the order of the B-spline. The order used in this work is $k_{\xi_1} = k_{\xi_2} = 2$, which is equivalent to a piecewise linear interpolation.[33] The expansion of the univariate B-splines for two Gaussian (zero mean, unit variance) random variables ξ_1 and ξ_2 is given by

$$\alpha(\xi_1) = \sum_{i=1}^{N_{\xi_1}} \hat{\alpha}_{i,\xi_1} B_{i,k_{\xi_1},\boldsymbol{x}_{\xi_1}}(\xi_1) \tag{11}$$

$$\alpha(\xi_2) = \sum_{j=1}^{N_{\xi_2}} \hat{\alpha}_{j,\xi_2} B_{j,k_{\xi_2},\boldsymbol{x}_{\xi_2}}(\xi_2) \tag{12}$$

where $\boldsymbol{x}_{\xi_1}$ is the vector of N_{ξ_1} knots on the ξ_1 axis and $\boldsymbol{x}_{\xi_2}$ is the vector of N_{ξ_2} knots on the ξ_2 axis. The multivariate B-spline is the tensor product of the two univariate B-splines and can be explicitly written as[33]

$$\alpha(\xi_1, \xi_2) = \sum_{i=1}^{N_{\xi_1}} \sum_{j=1}^{N_{\xi_2}} \hat{\alpha}_{ij} B_{j,k_{\xi_2},x_{\xi_2}}(\xi_2) B_{i,k_{\xi_1},x_{\xi_1}}(\xi_1) \tag{13}$$

The coefficient matrix, made up of the elements $\hat{\alpha}_{ij}$, is solved by repeated evaluations of the univariate spline interpolation problem, the details of which are given in de Boor.[33]

Now an efficient stochastic algorithm that is robust enough to identify bifurcations can be described. First, an interval is chosen in the stochastic domain over which samples of the LCO amplitude will be obtained. Next, the location of nodes to be sampled in that interval is determined. The multivariate B-spline that approximates the response surface in the stochastic domain is then determined. Finally, an MCS is performed on this response surface to estimate the PDF of the response. Each of the steps of this algorithm is now described in detail.

The interval selected is based on the distribution of random variables. For this work, the random variables have a Gaussian distribution. Strictly speaking, the interval defined for a Gaussian random variable is the whole real line. There is, however, a practical limit to this interval. The random variables control parametric uncertainties, and these parameters must be kept within specified bounds in order for the equations of motion to be numerically well behaved. In a real-world application the mean and standard deviation can be dictated by manufacturing, instrument error, or physical phenomena such as wind gusts. Because

$$\left(\frac{1}{\sqrt{2\pi}}\right)^2 \int_{-4}^{4}\int_{-4}^{4} e^{-\frac{1}{2}(\xi_1^2+\xi_2^2)}\,\mathrm{d}\xi_1\,\mathrm{d}\xi_2 \approx 0.99994 \tag{14}$$

that is, 99.99% of all responses occur on the interval $[-4, 4]$ in both stochastic axes, this was the interval selected for both the ξ_1 and ξ_2 axes to demonstrate the utility of the stochastic algorithm.

With the interval selected, nodes along the stochastic axis must be chosen that will efficiently capture the desired projection. For the B-spline to be valid over the entire interval, nodes must be selected that span the entire interval. However a Gaussian distribution of the nodes would cluster the nodes near the mean value, leaving a large gap between the Gaussian spaced nodes and the endpoints of the interval. Nodes at ± 4 are required to span the interval. Nodes at ± 2.5 are added to bridge the gap between the Gaussian spaced nodes and the endpoints of the interval. The Gaussian spaced nodes are determined by integration of the Gaussian PDF $w(\xi_1)$ or $w(\xi_2)$ [Eq. (5) with $d = 1$]. That is, the nodes are determined in one dimension, and the same nodes are used in the other dimension. The determination of the nodes proceeds as follows. Some number of nodes are selected on the interval $[0, 4]$. Let this number of nodes be represented by I along the ξ_1 axis and J along ξ_2 axis. Noting that

$$\int_0^4 \frac{1}{\sqrt{2\pi}} e^{-\frac{1}{2}\xi_1^2}\,\mathrm{d}\xi_1 \approx \frac{1}{2} \tag{15}$$

Table 1 Gaussian distributed nodes

$I = 2$	$I = 4$	$I = 8$
——	——	± 0.15731
——	± 0.31864	± 0.31684
——	——	± 0.48878
± 0.67449	± 0.67449	± 0.67449
——	——	± 0.88715
——	± 1.15035	± 1.15035
——	——	± 1.53412
± 2.5	± 2.5	± 2.5
± 4.0	± 4.0	± 4.0

the remaining nodes are selected based on equal intervals of the probabilities. For example, with $I = 2$ and one node fixed at $\xi_1 = 4$, the second node is determined from

$$\int_0^a \frac{1}{\sqrt{2\pi}} e^{-\frac{1}{2}\xi_1^2}\,\mathrm{d}\xi_1 = \frac{1}{4} \tag{16}$$

where a is the location of the node. A simple search leads to a value of $a = 0.67449$. Proceeding in a like manner for $I = 4$ and 8 leads to the node values given in Table 1. Because of the symmetry of the nodes and the extra nodes at $\xi_1 = \pm 2.5$, the total number of nodes along the ξ_1 stochastic axis is given by $2I + 2$.

Samples of the response are obtained at the selected values of ξ_1 and ξ_2. From these samples, the multivariate B-spline problem can be solved for the coefficient matrix $\hat{\alpha}_{ij}$ in Eq. (13). After these coefficients are determined, an MCS is performed on Eq. (13). It will be shown that this MCS is extremely efficient.

This algorithm fits into the stochastic projection framework through the following derivation, which parallels the development given by Eqs. (3–9). Consider the set of nodes $\boldsymbol{x}$ such that $x_i \in [-a, a]$ and $x_1 = -a < x_2 < \cdots < x_I = a$ for some integer I. Because it was noted that the preceding algorithm is a piecewise linear interpolation, the appropriate basis for expansion would be the hat function, which has the property[33]

$$\Psi_j(x_i) = \delta_{ij} \tag{17}$$

where δ_{ij} is the Dirac delta function. Additionally, $\delta_j(x) = \delta(x - x_j)$, which indicates sampling at a node. Just as the expected value operator was defined in Eq. (7) in order to integrate out the random variables, similar inner products with the trial basis δ_j and the weight function $w(x) = 1$ can be developed and are given by

$$\langle \Psi_i, \delta_j \rangle = \int_{-a}^{a} \Psi_i(x)\delta(x - x_j)\,\mathrm{d}x = \Psi_i(x_j) = \delta_{ij} \tag{18}$$

$$\langle x\Psi_i, \delta_j \rangle = \int_{-a}^{a} x\Psi_i(x)\delta(x - x_j)\,\mathrm{d}x = x_j\Psi_i(x_j) = x_j\delta_{ij} \tag{19}$$

The piecewise linear approximation to the response $\alpha(t, x)$ becomes

$$\alpha(t, x) = \sum_{i=1}^{I} \hat{\alpha}_i(t)\Psi_i(x) \tag{20}$$

and can be substituted into Eq. (3). By performing the stochastic projection and making use of the preceding inner products, the following system of equations result:

$$\mathcal{L}[\hat{\alpha}_j] + (\bar{\beta}_\alpha + x_j\tilde{\beta}_\alpha)\hat{\alpha}_j^3 = 0 \tag{21}$$

Thus, the samples of the random variable are used to obtain samples of the response, and a piecewise linear approximation to the response is obtained from the B-splines. Whereas the PCE method provides a best fit to the stochastic projection and converges, in the mean square sense, to an MCS,[34] the piecewise linear interpolation is exact at the nodes and, with a sufficient number of nodes, is a nearly optimal fit to an MCS.[33]

Fluid-Structure Coupling

Many researchers have demonstrated LCOs on typical airfoil sections with the inviscid Euler equations.[35–38] An inviscid aeroelastic code, EULER-AE, has been developed to investigate the response of a nonlinear airfoil in an inviscid transonic flow. The code is a finite volume formulation and is loosely coupled between the structure and fluid, that is, the structural dynamics lag the fluid dynamics by the integration time-step size. The airfoil selected for this study was the symmetric NACA 64A006 airfoil. This airfoil was investigated by Morton and Beran[35] to determine the flutter point of a linear airfoil in inviscid flow. The strategy of EULER-AE is to first attempt convergence to a steady-state solution at a fixed initial pitch angle. Once convergence or the maximum number of iterations is achieved, the airfoil is allowed to move subject to the lift and moment induced by the fluid flow. Some static cases of the airfoil at different angles of attack were computed with EULER-AE and compared against the commercial fluid solver FLUENT™ as well as experimental data.[39] A comparison with the parameters used by Morton and Beran to obtain an LCO for this airfoil is also presented.

The typical nondimensional parameters for the Euler equations are defined as[40]

$$x^* = x/c, \qquad y^* = y/c, \qquad u^* = u/V_\infty, \qquad v^* = v/V_\infty$$
$$\rho^* = \rho/\rho_\infty, \qquad p^* = p\big/\rho_\infty V_\infty^2$$
$$E_t^* = E_t\big/\rho_\infty V_\infty^2, \qquad t^* = t\,V_\infty/c \tag{22}$$

From this point the asterisk is dropped from the nondimensional parameters, and the primitive variables and grid locations are assumed to be nondimensional unless otherwise stated. The Euler equations in generalized coordinates with a moving grid are then given by[41]

$$\frac{\partial}{\partial t}\left(\frac{1}{J}\boldsymbol{Q}\right) + \frac{\partial}{\partial \xi}\left(\frac{1}{J}\boldsymbol{E}\right) + \frac{\partial}{\partial \eta}\left(\frac{1}{J}\boldsymbol{F}\right) = 0 \tag{23}$$

where

$$\boldsymbol{Q} = \begin{bmatrix} \rho \\ \rho u \\ \rho v \\ E_t \end{bmatrix}, \qquad \boldsymbol{E} = \begin{bmatrix} \rho U \\ \xi_x p + \rho U u \\ \xi_y p + \rho U v \\ (p + E_t)U - \xi_t p \end{bmatrix}$$

$$\boldsymbol{F} = \begin{bmatrix} \rho V \\ \eta_x p + \rho V u \\ \eta_y p + \rho V v \\ (p + E_t)V - \eta_t p \end{bmatrix} \tag{24}$$

An equation of state is required to close the system of equations. For an ideal gas with a constant ratio of specific heats γ, the equation of state is written as

$$E_t = p/(\gamma - 1) + \tfrac{1}{2}\rho(u^2 + v^2) \tag{25}$$

where $\gamma = 1.4$.

A two-stage explicit Runge–Kutta time integration with $\Delta t = 0.0002$ was employed.[32] The convective fluxes were computed from the flux-differencing Roe method[42] with a third-order discretization obtained from the monotone upstream-centered schemes for strong conservation laws[40] extrapolation. A MINMOD limiter was used to control overshoots.[40] The boundary conditions employed are described by Whitfield and Janus[43] with corrections made for the translation and rigid-body rotation of the computational domain.

The ordinates for the NACA 64A006 airfoil were obtained from the standard AGARD two-dimensional aeroelastic configurations.[44] The 257×65 computational domain is shown in Fig. 3. A close-up of the grid near the leading and trailing edges is shown in Fig. 4. The initial spacing on the leading edge was 0.00025 chords, and the spacing was allowed to increase slowly as the curvature decreased. The grid spacing was coarsest near the midpoint of the airfoil and then became more finely spaced near the trailing edge. The final grid

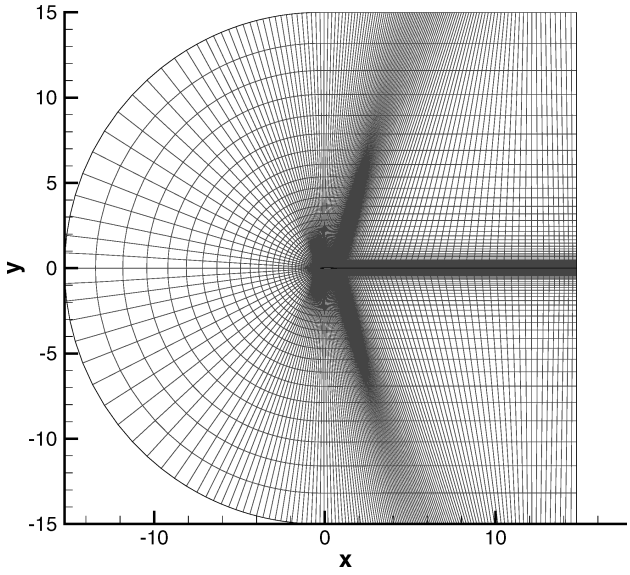

Fig. 3 NACA64A006 structured grid: far field.

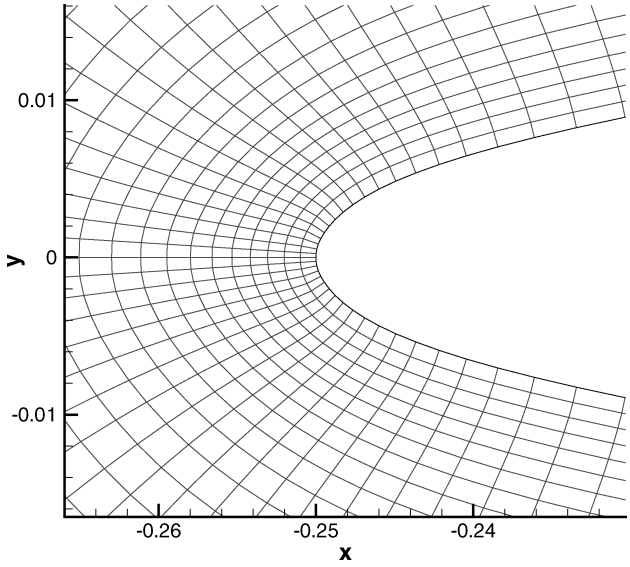

a) Leading edge

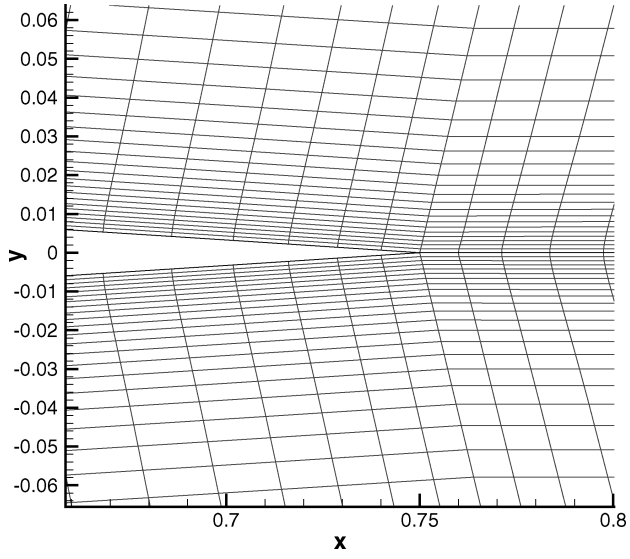

b) Trailing edge

Fig. 4 NACA64A006 structured grid: detail.

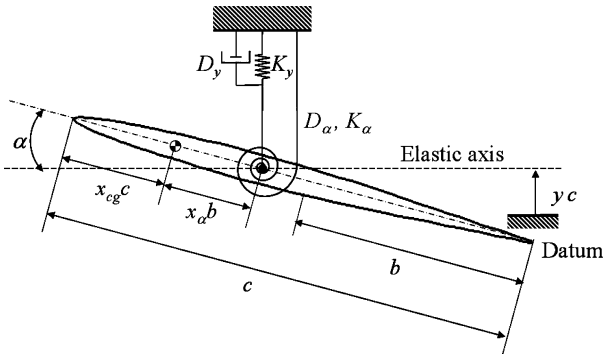

Fig. 5 Notation for the pitch and plunge airfoil used in EULER-AE.

point spacing at the trailing edge was approximately 0.01 chords. The initial grid spacing off the wall was 0.001 chords, and spacing exponentially increased out to 15 chord lengths.

The equations of motion for the nonlinear airfoil are based upon the equations derived by Morton and Beran[35] with the nomenclature shown in Fig. 5. Defining the additional nondimensional parameters

$$x^*_{\rm cg} = x_{\rm cg}/c, \qquad x^*_\alpha = x_\alpha/b, \qquad r^*_\alpha = r_\alpha/b$$

$$V_r = V_\infty/\omega_\alpha b, \qquad \omega_r = \omega_h/\omega_\alpha, \qquad \mu_s = m\big/\rho_\infty b^2\pi \quad (26)$$

the aeroelastic equations are given by (where again the asterisk is dropped for convenience)

$$\ddot{y} + (x_\alpha/2)\ddot{\alpha} + 4\zeta_y(\omega_r/V_r)\dot{y} + 4(\omega_r/V_r)^2 y = (2/\mu_s\pi)C_l \quad (27a)$$

$$x_\alpha\ddot{y} + \left(r^2_\alpha\big/2\right)\ddot{\alpha} + 2\zeta_\alpha\left(r^2_\alpha\big/V_r\right)\dot{\alpha} + 2\left(r^2_\alpha\big/V^2_r\right)\left(\alpha + \beta_\alpha\alpha^3 + \gamma_\alpha\alpha^5\right) = (4/\mu_s\pi)C_m \quad (27b)$$

where β_α is the cubic spring constant and γ_α is the quintic spring constant. By letting

$$\boldsymbol{S} = \begin{pmatrix} s_1 \\ s_2 \\ s_3 \\ s_4 \end{pmatrix} = \begin{pmatrix} \alpha \\ \dot{\alpha} \\ y \\ \dot{y} \end{pmatrix} \quad (28)$$

the equations of motion can be written in the compact notation

$$[M]\dot{\boldsymbol{S}} + [K_1]\boldsymbol{S} + [K_3]\boldsymbol{S}^3 + [K_5]\boldsymbol{S}^5 = \boldsymbol{G} \quad (29)$$

where

$$[M] = \begin{bmatrix} 1 & 0 & 0 & 0 \\ 0 & \dfrac{x_\alpha}{2} & 0 & 1 \\ 0 & 0 & 1 & 0 \\ 0 & \dfrac{r^2_\alpha}{2} & 0 & x_\alpha \end{bmatrix}$$

$$[K_1] = \begin{bmatrix} 0 & -1 & 0 & 0 \\ 0 & 0 & 4\left(\dfrac{\omega_r}{V_r}\right)^2 & 4\zeta_y\dfrac{\omega_r}{V_r} \\ 0 & 0 & 0 & -1 \\ \dfrac{r^2_\alpha}{V^2_r} & 2\zeta_\alpha\dfrac{r^2_\alpha}{V_r} & 0 & 0 \end{bmatrix} \quad (30a)$$

$$[K_3] = \begin{bmatrix} 0 & 0 & 0 & 0 \\ 0 & 0 & 0 & 0 \\ 0 & 0 & 0 & 0 \\ 2\dfrac{r^2_\alpha}{V^2_r}\beta_\alpha & 0 & 0 & 0 \end{bmatrix}, \qquad [K_5] = \begin{bmatrix} 0 & 0 & 0 & 0 \\ 0 & 0 & 0 & 0 \\ 0 & 0 & 0 & 0 \\ 2\dfrac{r^2_\alpha}{V^2_r}\gamma_\alpha & 0 & 0 & 0 \end{bmatrix} \quad (30b)$$

$$\boldsymbol{G} = \begin{pmatrix} 0 \\ f \\ 0 \\ g \end{pmatrix} = \begin{pmatrix} 0 \\ \dfrac{2}{\mu_s\pi}C_l \\ 0 \\ \dfrac{4}{\mu_s\pi}C_m \end{pmatrix} \quad (30c)$$

Solving for $\dot{\boldsymbol{S}}$ yields

$$\dot{\boldsymbol{S}} = [M]^{-1}\left(\boldsymbol{G} - [K_1]\boldsymbol{S} - [K_3]\boldsymbol{S}^3 - [K_5]\boldsymbol{S}^5\right) \quad (31)$$

which fully expanded becomes

$$\begin{pmatrix} \dot{s}_1 \\ \dot{s}_2 \\ \dot{s}_3 \\ \dot{s}_4 \end{pmatrix} = \begin{pmatrix} s_2 \\ \dfrac{2}{r^2_\alpha - x^2_\alpha}[g_1 - x_\alpha f_1] \\ s_3 \\ \dfrac{1}{r^2_\alpha - x^2_\alpha}\left[r^2_\alpha f_1 - x_\alpha g_1\right] \end{pmatrix} \quad (32)$$

where

$$f_1 = f - 4(\omega_r/V_r)^2 s_3 - 4\zeta_y(\omega_r/V_r)s_4 \quad (33a)$$

$$g_1 = g - 2\left(r^2_\alpha\big/V^2_r\right)\left(s_1 + \beta_\alpha s^3_1 + \gamma_\alpha s^5_1\right) - 2\zeta_\alpha\left(r^2_\alpha\big/V_r\right)s_2 \quad (33b)$$

Equation (32) is also integrated explicitly in time by the two-stage Runge–Kutta method.

Two static cases and an LCO case are presented as validation of the research code. This validation is necessary to gain confidence in EULER-AE before demonstrating the applicability of the stochastic projection method via B-splines. The static cases are compared with results from FLUENT and experimental data.[39] The first case was run at $M_\infty = 0.86$ and $\alpha = 0$, and the second case was run at $M_\infty = 0.85$ and $\alpha = 4$ deg. The resulting pressure distributions are shown in Fig. 6. Both EULER-AE and FLUENT are in very good agreement with one another. The predicted shock locations are one cell different between the two codes. This is probably caused by EULER-AE being run with a third-order spacial scheme, while FLUENT is limited to a second-order scheme. The difference in order of spatial discretization also explains why the shock is more sharply defined with EULER-AE. As expected, the inviscid shocks are stronger and further aft on the wing than the experimental data, especially at large angles of attack (Fig. 6b). This will lead to a prediction of a much larger lift coefficient for the inviscid cases. Although comparison with the experimental data is only fair, because of the lack of viscous and turbulence modeling, the code-to-code comparison with FLUENT indicates that EULER-AE properly predicts an inviscid flow over the airfoil.

The time-accurate fluid-structure interaction was verified by comparing with an LCO prediction given by Morton and Beran.[35] A complete validation was not possible because of the different formulations of EULER-AE and Morton and Beran.[35] EULER-AE employs a matched-point analysis, whereas the method of Morton and Beran[35] employs a nonmatched-point analysis. A matched-point analysis ensures the reduced velocity, freestream air density, and freestream Mach number are consistent with standard atmospheric conditions.[45] A given density and Mach number implies a freestream velocity, which in turn implies the values of the uncoupled natural frequencies of pitch and plunge, as shown in Eq. (26). Thus, the amplitude and frequency of the coupled response from a matched-point and nonmatched-point analysis will not necessarily be the same.

Morton and Beran[35] use the following parameters to obtain an LCO from the NACA 64A006 airfoil with linear pitch ($\beta_\alpha = \gamma_\alpha = 0$) and plunge springs:

$$x_{\rm cg} = 0.375, \qquad x_\alpha = -0.25, \qquad r^2_\alpha = 0.25, \qquad M_\infty = 0.85$$
$$\mu_s = 125, \qquad \omega_r = 0.2, \qquad \zeta_y = 0.5, \qquad \zeta_\alpha = 0.5 \quad (34)$$

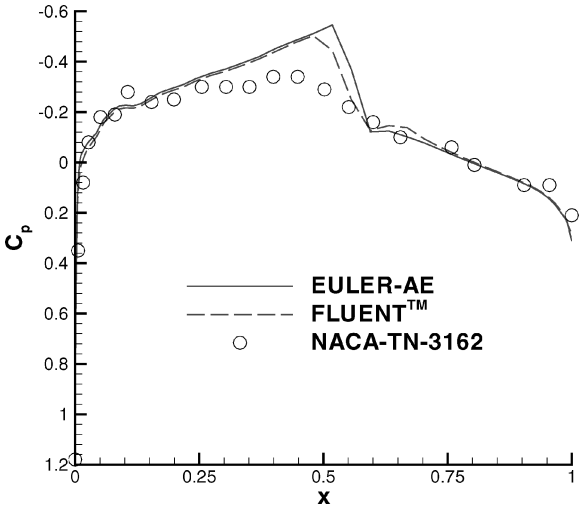

a) $M_\infty = 0.86$; $\alpha = 0$

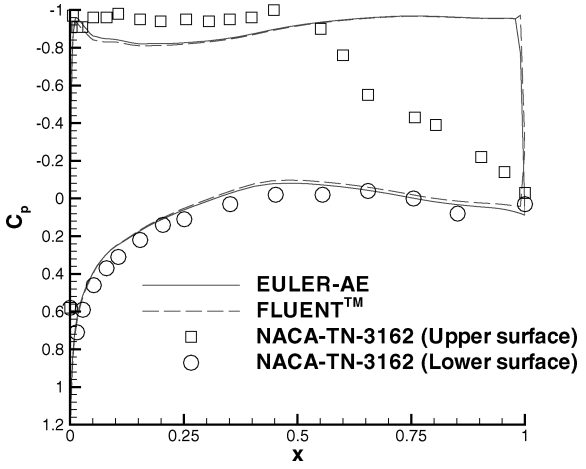

b) $M_\infty = 0.85$; $\alpha = 4$ deg

Fig. 6 Pressure distributions on the NACA 64A006 airfoil.

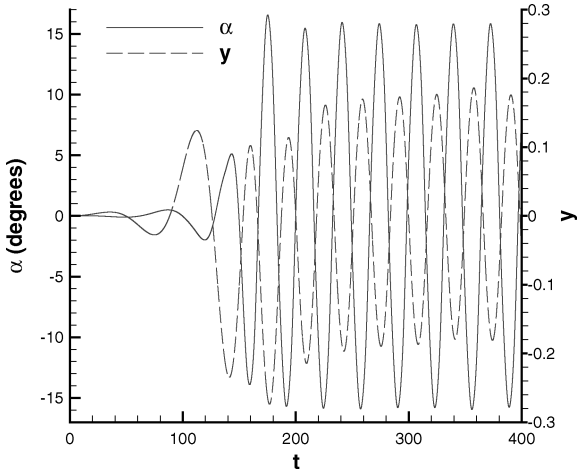

Fig. 7 LCO at $V_r = 11.0$.

At a reduced velocity of $V_r = 11$ and standard sea-level conditions ($p_\infty = 101{,}325$ N/m^2 and $\rho_\infty = 1.225$ kg/m^3), EULER-AE predicts the pitch and plunge LCOs shown in Fig. 7. Table 2 shows the difference between the results from EULER-AE and Mortan and Beran.[35] The shorter period from EULER-AE indicates that the pitch spring stiffness for the aeroelastic system is greater than that from Morton and Beran.[35] However, the larger amplitudes in pitch and, especially, plunge indicate just the opposite. The reason for the

Table 2 Differences between LCOs from EULER-AE and Morton and Beran[35]

Method	α_{LCO}, deg	y_{LCO}	Period	Flutter point
EULER-AE	15.8	0.176	32.9	6.78
Ref. 35	13.0	0.020	61.6	10.28

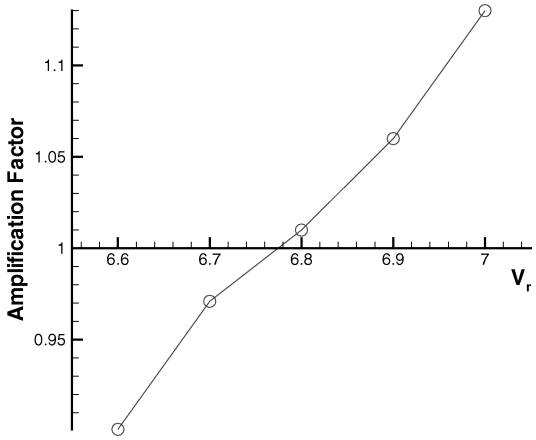

Fig. 8 Flutter point estimation.

apparent discrepancy, as will demonstrated, is the flutter point for the matched-point aeroelastic system is located at a much lower reduced velocity ($V_r \approx 6.78$) than that of the nonmatched-point aeroelastic system ($V_r = 10.28$) (Ref. 35).

Results

A typical aeroelastic simulation performed by EULER-AE took approximately 36 to 48 h to reach a fully developed LCO, making the MCS approach of determining PDFs of a response impractical. The stochastic projection method via B-plines was applied to the aeroelastic system to determine the subcritical response[46] of the NACA 64A006 airfoil. The subcritical case was examined because LCOs can be obtained below the classically defined flutter point, representing a greater risk to an aircraft and aircrew.[8] The following discussion begins by demonstrating the selection of parameters to obtain a subcritical response of the aeroelastic system. Once the parameters are chosen, nodes are sampled along each stochastic axis to determine the resolution required to obtain accurate PDFs of the response. A further refinement of the nodes is then presented to demonstrate convergence of the stochastic algorithm. Finally, the probability of failure is estimated from the computed PDFs.

Nonlinear structural parameters were chosen for the NACA 64A006 airfoil to produce a subcritical response with a turning point. Care was taken to choose parameters such that pitch and plunge excursions were still valid in the context of an Euler code, that is, small-amplitude LCOs. With the parameters chosen, the flutter point, turning point, and bifurcation diagram were estimated from numerous computer runs. The bifurcation diagram of the nonlinear aeroelastic system was determined first. Development of the bifurcation diagram began with an estimation of the flutter point. The flutter point is a loss of linear stability, and its location is unaffected by the nonlinear parameters. Gordnier and Melville[7] efficiently estimated the flutter point of an aeroelastic system by first computing a few cycles at reduced velocities above and below the flutter point and then comparing amplitude factors as the cycles either increase or decrease. The amplitude factor is defined as the ratio of the peak magnitude with the magnitude of the previous peak with the same sign (i.e., one period).[7] The parameters given in Eq. (34) with $\beta_\alpha = \gamma_\alpha = 0$ provided a supercritical response from which the flutter point could be estimated. With an initial pitch of $\alpha(0) = 0.1$ deg, cases were run at reduced velocities of $V_r = 6.6$, 6.7, 6.8, 6.9, and 7.0. An average of the last few amplification factors for each of the responses resulted in the plot shown in Fig. 8. From Fig. 8 the flutter point is estimated to occur at $V_r \approx 6.78$.

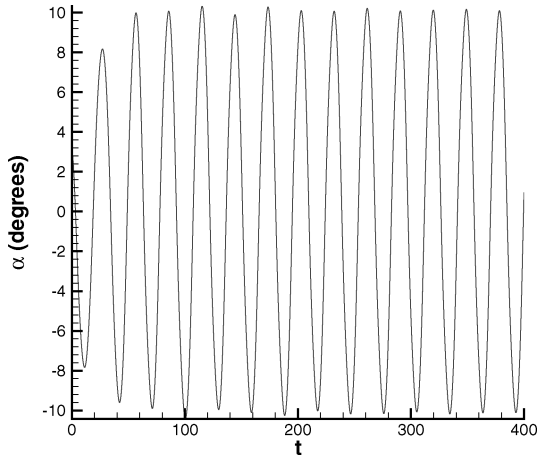

Fig. 9 LCO caused by a subcritical response; $V_r = 6.5$, $\alpha(0) = 3$ deg, $\beta_\alpha = -30$, and $\gamma_\alpha = 500$.

Once the flutter point was determined, nonlinear parameters were selected to produce a subcritical response with a turning point. Following Millman et al.,[27] the cubic spring constant of $\beta_\alpha < 0$ was chosen to destabilize the aeroelastic system below the flutter point. The goal here was to choose a β_α such that the aeroelastic system was destabilized at a small initial pitch angle. Numerical experimentation led to a value of $\beta_\alpha = -30$, which caused the aeroelastic system to become unstable with $\alpha(0) \approx 3$ deg at a reduced velocity of $V_r = 6.5$. The quintic spring constant γ_α was then chosen to restabilize the system. Again through numerical experimentation, a value of $\gamma_\alpha = 500$ was selected. This value resulted in a LCO at $V_r = 6.5$ with an initial pitch angle of $\alpha(0) = 3$ deg, as shown in Fig. 9. For clarity, the parameters of the aeroelastic system are presented again. The structural parameters, with the inclusion of the nonlinear spring constants, are

$$x_{\text{cg}} = 0.375, \qquad x_\alpha = -0.25, \qquad r_\alpha^2 = 0.25$$
$$\mu_s = 125, \qquad \zeta_y = 0.5, \qquad \zeta_\alpha = 0.5$$
$$\omega_r = 0.2, \qquad \beta_\alpha = -30, \qquad \gamma_\alpha = 500 \tag{35}$$

and the aerodynamic parameters are

$$p_\infty = 37{,}612\ \text{N/m}^2, \qquad \rho_\infty = 0.5489\ \text{kg/m}^3, \qquad M_\infty = 0.85 \tag{36}$$

The freestream pressure and density correspond to an altitude of 25,000 ft.

With the parameters chosen, numerous computer runs were conducted on a range of reduced velocities at and below the flutter point to map out the subcritical bifurcation. In each case a sufficiently large initial pitch angle of $\alpha(0) = 7$ deg was chosen to ensure the aeroelastic system would exhibit LCO. It was found that the system would rapidly exhibit LCO or rapidly proceed to a stationary response near the turning point, as shown in Fig. 10.

The turning point was estimated at $V_r \approx 6.11$. The resulting bifurcation diagram is shown in Fig. 11.

An initial condition uncertainty and a parametric uncertainty are now added to the formulation. A Gaussian distribution in the uncertainties was assumed. These uncertainties are given by

$$\alpha(0) = \bar{\alpha}(0) + \xi_1 \tilde{\alpha}(0) \tag{37a}$$

$$\beta_\alpha = \bar{\beta}_\alpha + \xi_2 \tilde{\beta}_\alpha \tag{37b}$$

For this aeroelastic system, the following mean and standard deviation values were used:

$$\bar{\alpha}(0) = 0, \qquad \bar{\beta}_\alpha = -30 \tag{38a}$$

$$\tilde{\alpha}(0) = 1.5\,\text{deg}, \qquad \tilde{\beta}_\alpha = 3 \tag{38b}$$

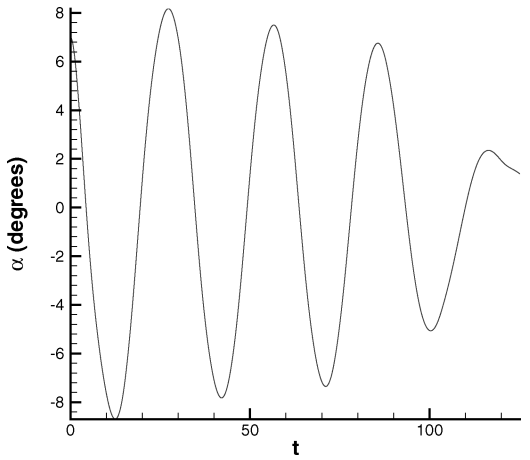

a) $V_r = 6.105$; $\alpha(0) = 7$ deg

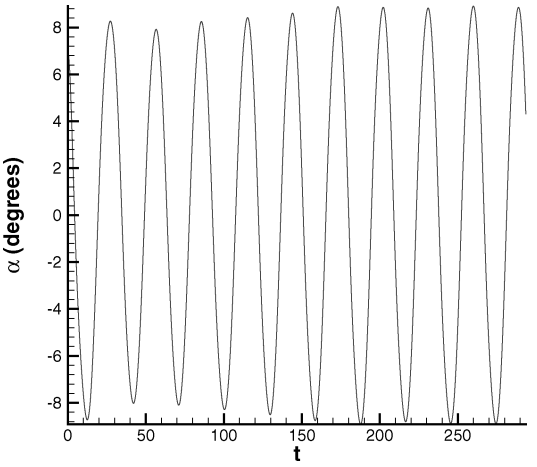

b) $V_r = 6.115$; $\alpha(0) = 7$ deg

Fig. 10 Identification of the turning point.

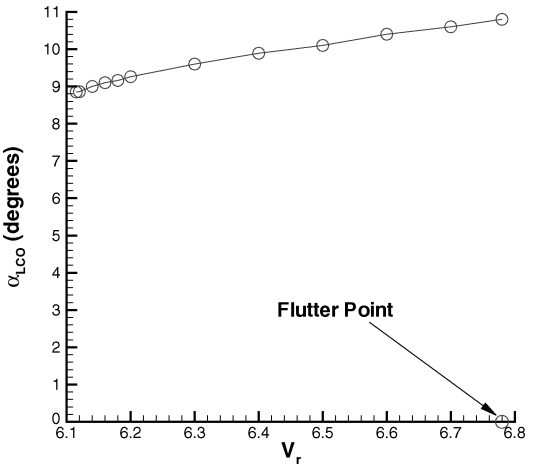

Fig. 11 Bifurcation diagram for the nonlinear aeroelastic system.

Samples of the responses in pitch, plunge, and frequency were obtained at the nodes given in Table 1 at a reduced velocity of $V_r = 6.5$.

The effect of increasing resolution on the ξ_2 axis (uncertainty in the cubic spring constant) as the resolution on the ξ_1 axis (uncertainty in the initial pitch angle) remained fixed was investigated first. Each simulation was carried out to $t_{\max} \approx 500$ or until the LCO became fully developed. The samples obtained from the simulations were used to build the B-spline (piecewise linear) surfaces from Eq. (13). An example of the resulting surfaces is shown in Fig. 12.

Immediately of note from the B-spline surface in Fig. 12 is that, as in the model problem, the symmetric airfoil and the zero mean

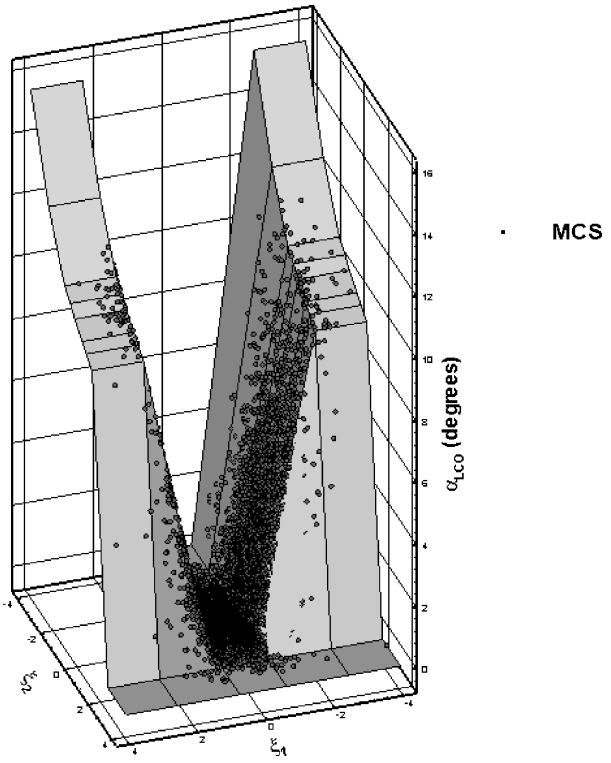

Fig. 12 B-spline surface of the pitch response ($I = 2, J = 8$).

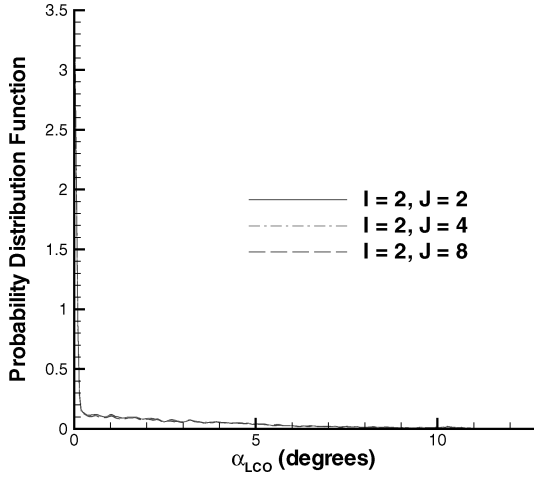

a) PDFs of the pitch response

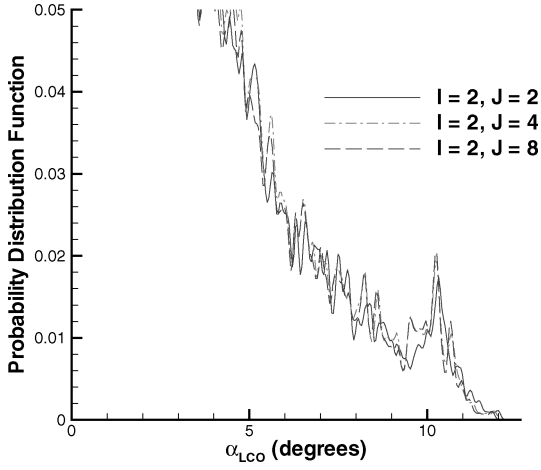

b) Close up of PDFs of the pitch response

Fig. 13 Pitch response.

initial pitch angle lead to symmetry on the ξ_1 axis. Also, if an LCO develops for a given set of structural parameters, the amplitude of the LCO is the same regardless of the initial pitch angle. These two properties of the B-spline surface for this aeroelastic system can lead to a reduction in both the number and the computational effort of simulations as the resolution increases in either axis. It will be noted later in the discussion when these properties were invoked.

A bifurcation is observed on the ξ_2 axis. This bifurcation occurs between $\xi_2 = 1.53415$ and $\xi_2 = 2.5$. This corresponds to

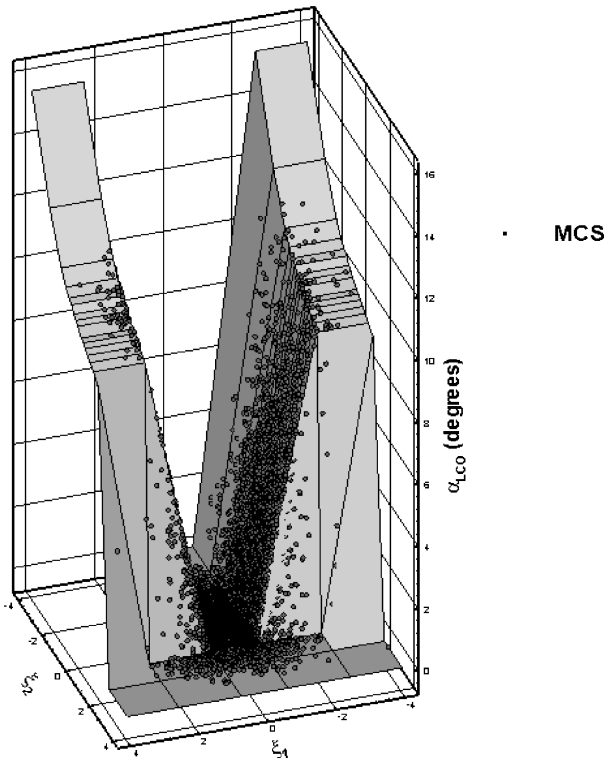

a) $I = 2, J = 4$

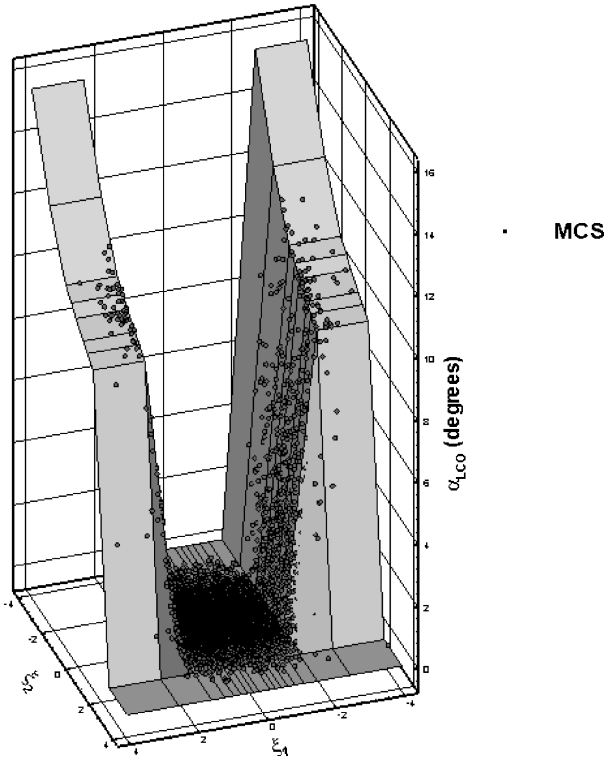

b) $I = 8, J = 4$

Fig. 14 B-spline surfaces of the pitch response (α_{LCO}).

$\beta_\alpha = -25.398$ and -22.5, respectively. Thus, as the overall pitch spring stiffness becomes greater, that is, less destabilization from the cubic spring constant, LCO will not develop for any initial pitch angle. This is an example of how uncertainty in the structural components has an effect on the LCO of an aeroelastic system.

Also shown on Fig. 12 are the results of a 10,000 MCS obtained from the B-spline surface. (Note: Ten-thousand randomly generated Gaussian variables can occasionally, although rarely, exceed the interval $[-4, 4]$. When this occurred, the value of that random variable was mapped to the closest boundary.) As expected, the MCS samples are concentrated near the zero means. Because the discontinuities associated with the bifurcations are not sharply resolved, many realizations fall on values intermediate to the stationary response and the LCO response. The effect of these intermediate values can be seen in the PDFs of the response shown in Fig. 13. These PDFs were estimated from a Parzen windowing approach.[47] Because the bulk of intermediate values is a result of the poor resolution in the ξ_1 axis, increasing resolution in the ξ_2 axis had little effect on the the convergence of the PDF of the pitch response. A very close examination reveals that with $J = 4$ and 8 the PDFs are essentially identical. Further investigation of the uncertainty quantification is, therefore, continued holding the resolution in the ξ_2 axis fixed at $J = 4$.

Having examined the stochastic response surface with increasing resolution along the ξ_2 axis, simulations were then performed with increasing resolution on the ξ_1 axis. Because the amplitudes of the LCOs were already known from the preceding set of simulations, these simulations were carried out just far enough in time to determine if an LCO were developing or if the response were damped ($t_{\max} < 250$). Examples of the resulting B-spline surfaces are shown in Fig. 14. As the resolution increases, the discontinuity is more sharply refined. This refinement leads to fewer realizations intermediate to the LCO and the stationary responses.

As expected, the fewer intermediate realizations lead to a better estimates of the PDFs of the response, as shown in Fig. 15. With each increase in resolution, the PDFs show fewer intermediate realizations while an area near $\alpha_{\text{LCO}} \approx 10$ deg remains unchanged. Note that from Fig. 11 the mean response at $V_r = 6.5$ is $\alpha_{\text{LCO}} = 10.1$ deg. Thus, from these simulations it is estimated that a bimodal response exists with the primary response at $\alpha_{\text{LCO}} = 0$ and the secondary response at $\alpha_{\text{LCO}} = 10$ deg. Additionally, the uncertainty bounds for the secondary response are estimated to be from $\alpha_{\text{LCO}} = 9$ to 12 deg. The subcritical response and the uncertainty bounds were identified with a sample size of 180 simulations.

A better estimate of the subcritical response can easily be obtained by making use of the information already gained. The locations of the bifurcations have been bounded and with a simple binary search can be better refined. Further validation of this method can also be shown by refining the B-spline surface at a different set of nodes. Thus the nodes chosen along the ξ_2 axis were uniformly spaced until reaching the bifurcation while the nodes along the ξ_1 were selected to refine the bifurcations on that axis. Additionally, only the positive half of the ξ_1 axis was investigated, and symmetry was assumed on the negative half of the axis. A few simulations were conducted to verify this symmetry. With the preceding assumptions, approximately 100 simulations were performed to obtain the nodes for the refined B-spline shown in Table 3. Because the nodes no longer

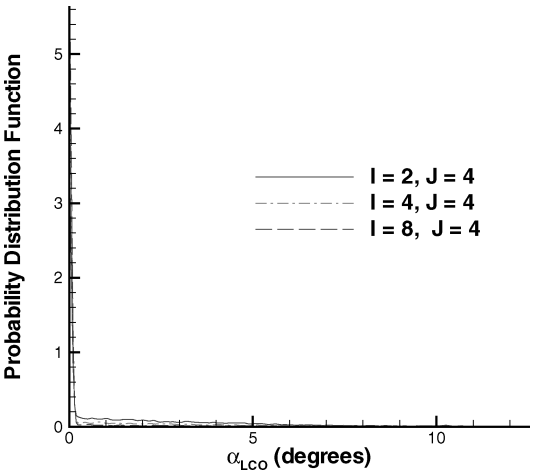

a) PDFs of the pitch response

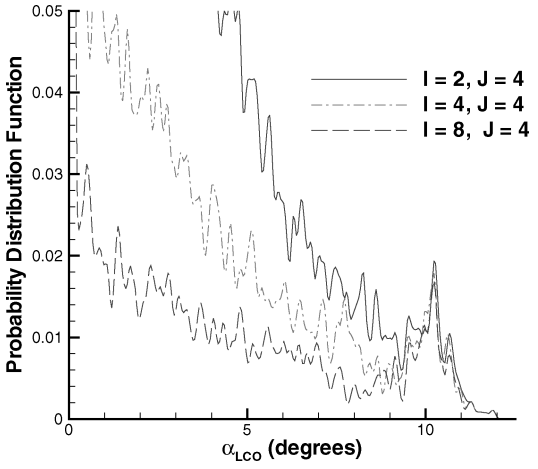

b) Close-up of PDFs of the pitch response

Fig. 15 Pitch response.

Table 3 Nodes for the refined B-spline surface

ξ_1	ξ_2	α_{LCO}, deg	ξ_1	ξ_2	α_{LCO}, deg	ξ_1	ξ_2	α_{LCO}, deg
−4	−4	15.6	−4	−1	10.9	−4	2.03333	8.89
−1.7	——	15.6	−1.83667	——	10.9	−3.26	——	8.89
−1.69667	——	0	−1.83333	——	0	−3.25667	——	0
1.69667	——	0	1.83333	——	0	3.25667	——	0
1.7	——	15.6	1.83667	——	10.9	3.26	——	8.89
4	——	15.6	4	——	10.9	4	——	8.89
−4	−3	13.9	−4	0	10.1	−4	2.06666	0
−1.73	——	13.9	−1.91667	——	10.1	−3.26	——	0
−1.72667	——	0	−1.91333	——	0	−3.25667	——	0
1.72667	——	0	1.91333	——	0	3.25667	——	0
1.73	——	13.9	1.91667	——	10.1	3.26	——	0
4	——	13.9	4	——	10.1	4	——	0
−4	−2	12.0	−4	1	9.53	−4	4	0
−1.78	——	12.0	−2.04	——	9.53	−3.26	——	0
−1.77667	——	0	−2.03667	——	0	−3.25667	——	0
1.77667	——	0	2.03667	——	0	3.25667	——	0
1.78	——	12.0	2.04	——	9.53	3.26	——	0
4	——	12.0	4	——	9.53	4	——	0

compose a regular mesh, the multivariate B-spline approach is difficult to implement. The 10,000-run MCS is accomplished by a simple linear interpolation scheme, which is equivalent to a piecewise linear approximation of the second order B-spline.[33] A comparison of the B-spline surface obtained with $I = 8$ and $J = 4$ with the refined B-spline surface and the associated MCS realizations is shown in Fig. 16. A PDF of the pitch response obtained from the refined B-spline surface is seen to achieve convergence in Fig. 17, where the

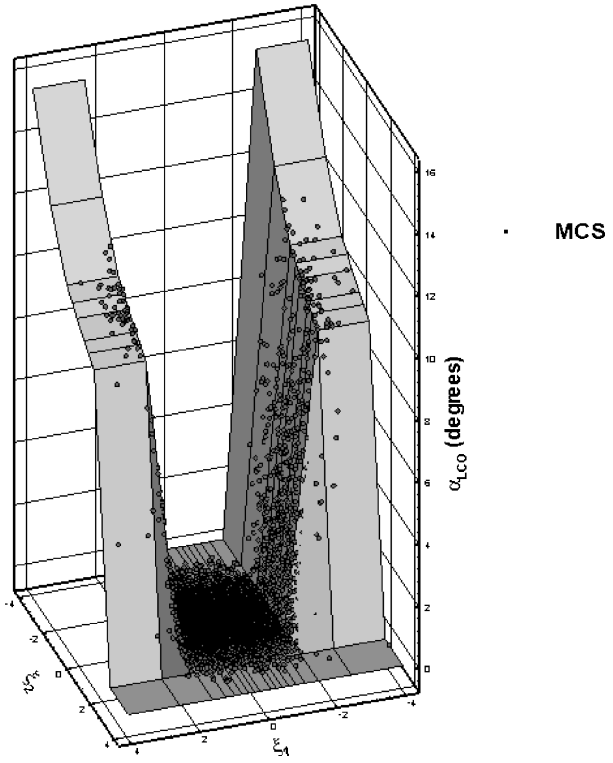

a) B-spline surface from the Gaussian nodes ($I = 8, J = 4$)

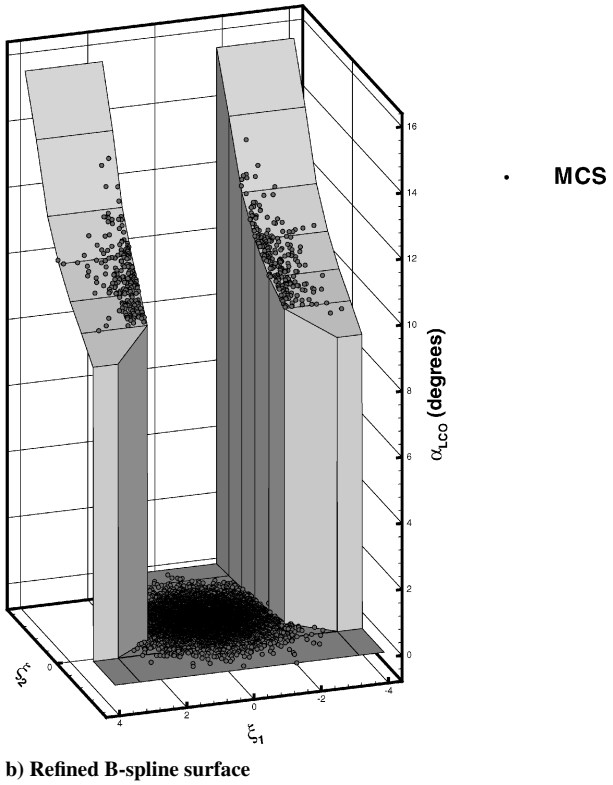

b) Refined B-spline surface

Fig. 16 Pitch response.

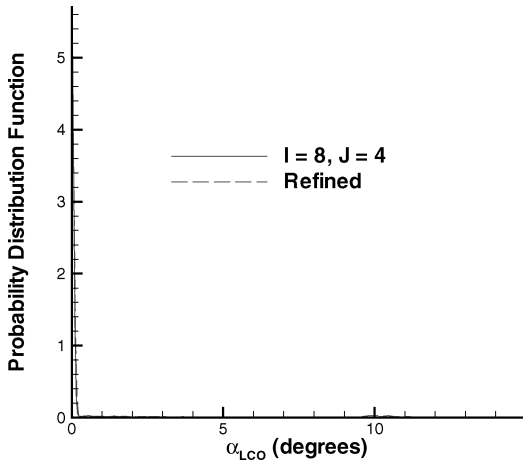

a) PDFs of the pitch response

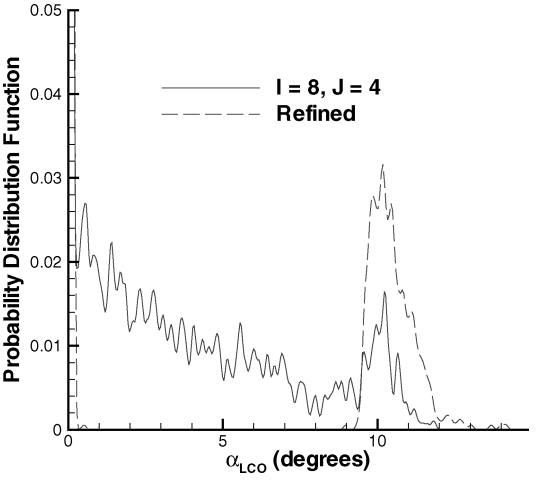

b) Close-up of PDFs of the pitch response

Fig. 17 Convergence of the pitch subcritical response.

intermediate values between the stationary response and the LCO response are practically nonexistent.

The same uncertainty analysis was investigated for the plunge LCO amplitude and the coupled frequency. B-spline surfaces of the plunge LCO amplitude y_{LCO} and the coupled frequency ω_{LCO} were developed for both the $I = 8$ and $J = 4$ Gaussian nodes as well as with the refined nodes. Convergence of the PDFs for these responses is shown in Figs. 18 and 19.

The PDFs of the LCO responses allow an estimate the probability of failure for the aeroelastic system. Certain criteria need to be chosen that define the failure mode. Recalling that the subcritical LCO develops below the flutter point, failure is defined as the onset of an LCO. To perform the integration of the PDFs and to avoid the smoothing error inherent in the Parzen windowing approach, failure in each mode (pitch, plunge, and frequency) was set at

$$\alpha_{\text{fail}} = 1 \text{ deg} \tag{39a}$$

$$y_{\text{fail}} = 0.01 \tag{39b}$$

$$\omega_{\text{fail}} = 1 \text{ Hz} \tag{39c}$$

With these failure modes defined, the probability of failure was estimated from the PDFs obtained from the Gaussian nodes as well as from the refined nodes. The results are summarized in Table 4. As resolution increases, the estimation of the probability of failure improves until, at the refined surface, all three probability of failures converge to the same value. The convergence of all three probabilities of failure to the same value is an expected result because the three events (pitch, plunge, and frequency) are not independent of each other. If the aeroelastic system experiences a pitch (plunge)

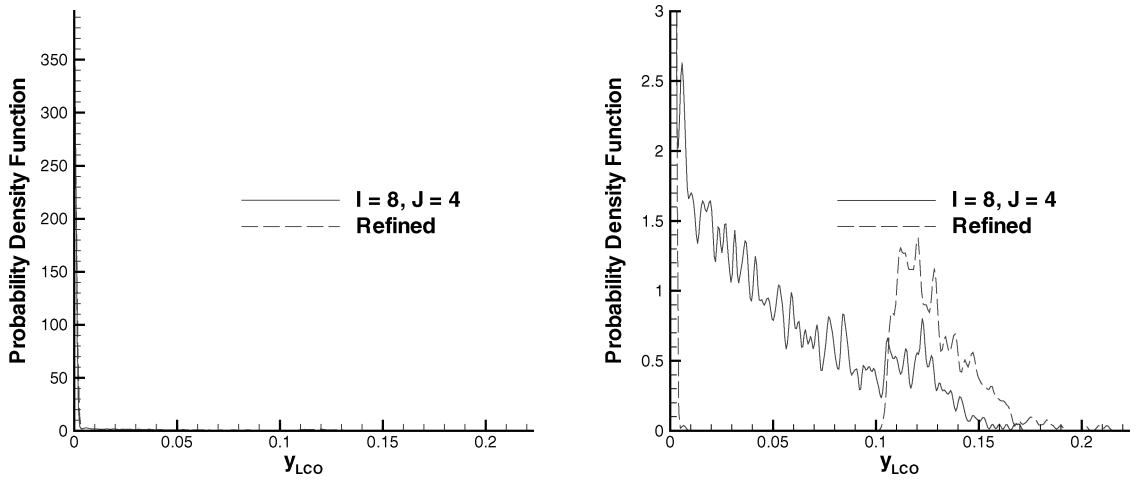

a) PDFs of the plunge response b) Close-up of PDFs of the plunge response

Fig. 18 Convergence of the plunge subcritical response.

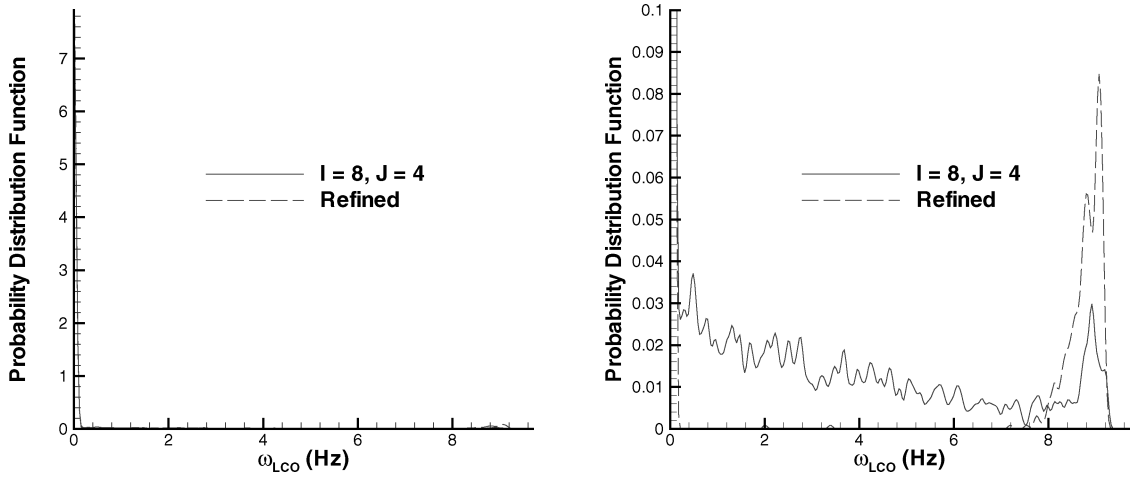

a) PDFs of the plunge response b) Close-up of PDFs of the plunge response

Fig. 19 Convergence of the frequency subcritical response.

Table 4 Estimates of the probability of failure

	Probability of failure,%		
Nodes	Pitch	Plunge	Frequency
$I=2$, $J=4$	38.1	39.7	36.9
$I=4$, $J=4$	19.6	20.3	18.9
$I=8$, $J=4$	10.3	10.6	10.1
Refined	4.36	4.36	4.36

LCO, it must also exhibit a plunge (pitch) LCO, and these LCOs will occur at some frequency. Because of the numerous realizations at the intermediate values, the Gaussian nodes provide a conservative estimate of the probability of failure while the refined nodes provide an estimate on the order of a full-up MCS. The total number of actual simulations performed, however, are two orders of magnitude less than that of a 10,000-run MCS.

Conclusions

The probability of failure of an aeroelastic system was shown to be sensitive to variations in both initial condition and structural parameter uncertainties and was computed from an estimated probability density function (PDF) of a subcritical response without performing a monte carlo simulation on the full nonlinear system. To estimate the PDF of the subcritical response, a stochastic algorithm based upon the polynomial chaos and Fourier chaos expansions stochastic projection methods was developed by employing multivariate B-splines. This method is a nonintrusive (sampling) approach that does not require the computation or storage of expected values to estimate the stochastic projection of the response. Instead, the B-spline approach is a collocation method that fits a surface to the nodes provided. The nodes were selected both by a Gaussian distribution as well as a uniform distribution of probabilities.

The applicability of the stochastic algorithm was investigated for the computationally demanding Computational-fluid-dynamics (CFD) simulation of an aeroelastic system. An inviscid aeroelastic code (EULER-AE) was developed, verified, and validated to perform this investigation. Parameters were selected to obtain a subcritical response with a turning point. This response is considered high risk because large-amplitude limit-cycle oscillations can develop below the classically defined flutter point. Monte Carlo simulations were impractical for this problem because each simulation took 36 to 48 h to perform. Validity of the stochastic projection method via B-splines was determined by convergence of the PDFs and the probability of failure. Efficiency was two orders of magnitude greater than that of the Monte Carlo approach, making this stochastic algorithm applicable to large time, CFD applications.

Acknowledgments

This project was sponsored and funded by the Air Force Research Laboratory, AFRL/VASD, Wright–Patterson Air Force Base. The views expressed in this paper are those of the authors and do not reflect the official policy or position of the United States Air Force, the Department of Defense, or the U.S. Government.

References

[1]Fung, Y., *An Introduction to the Theory of Aeroelasticity*, Dover, New York, 1969, pp. 160–185.

[2]Bunton, R. W., and Denegri, C. M., "Limit Cycle Oscillation Characteristics of Fighter Aircraft," *Journal of Aircraft*, Vol. 37, No. 5, 2000, pp. 916–918.

[3]Lee, B., Jiang, L., and Wong, Y., "Flutter of an Airfoil with a Cubic Nonlinear Restoring Force," AIAA Paper 98-1725, April 1998.

[4]Matsushita, H., Saitoh, K., and Gránásy, P., "Wind Tunnel Investigation of Transonic Limit Cycle Oscillation," AIAA Paper 98-1725, April 1998.

[5]Tang, L., Bartels, R., Chen, P., and Liu, D., "Simulation of Transonic Limit Cycle Oscillation Using a CFD Time Marching Method," AIAA Paper 2001-1292, April 2001.

[6]Beran, P., "Computation of Limit Cycle Oscillation Using a Direct Method," AIAA Paper 99-1462, April 1999.

[7]Gordnier, R. E., and Melville, R. B., "Transonic Flutter Simulations Using an Implicit Solver," *Jounal of Aircraft*, Vol. 37, No. 5, 2000, pp. 872–879.

[8]Beran, P. S., and Pettit, C. L., "A Direct Method for Quantifying Limit Cycle Oscillation Response Characteristics in the Presence of Uncertainties," AIAA Paper 2004-1695, April 2004.

[9]Grigoriu, M., *Stochastic Calculus: Applications in Science and Engineering*, Birkhäuser, Boston, 2002, Chap. 9.

[10]Ibrahim, R., "Structural Dynamics with Parameter Uncertainties," *Applied Mechanics Review*, Vol. 40, No. 3, 1987, pp. 309–328.

[11]Manohar, C., and Ibrahim, R., "Progress in Structural Dynamics with Stochastic Parameter Variations," *Applied Mechanics Review*, Vol. 52, No. 5, 1999, pp. 177–197.

[12]Beran, P., and Silva, W., "Reduced Order Modeling: New Approaches to Computational Physics," AIAA Paper 2001-0853, Jan. 2001.

[13]Beran, P. S., and Pettit, C. L., "Prediction of Nonlinear Panel Response Using Proper Orthogonal Decomposition," AIAA Paper 2001-1292, April 2001.

[14]Pettit, C. L., and Beran, P. S., "Reduced-Order Modeling for Flutter Prediction," AIAA Paper 2000-1446, April 2000.

[15]Wiener, N., "The Homogeneous Chaos," *American Journal of Mathematics*, Vol. 60, 1938, pp. 897–936.

[16]Cameron, R., and Martin, W., "The Orthogonal Development of Nonlinear Functionals in Series of Fourier-Hermite Functionals," *Annals of Mathematics*, Vol. 48, 1947, pp. 385–392.

[17]Ghanem, R. G., and Spanos, P. D., *Stochastic Finite Element Methods: A Spectral Approach*, Springer-Verlag, New York, 1991, Chap. 2.

[18]Ghanem, R., "A Comparative Analysis of FORM/SORM and Polynomial Chaos Expansions for Highly Nonlinear Systems," *Engineering Mechanics: Proceedings of the 11th Conference*, edited by Y. Lin and D. Ghiocel, Vol. 1, Engineering Mechanics Div. of ASCE, American Society of Civil Engineers, New York, 1996, pp. 535–538.

[19]Li, R., and Ghanem, R., "Adaptive Polynomial Chaos Expansions Applied to Statistics of Extremes in Non-Linear Random Vibration," *Probabilistic Engineering Mechanics*, Vol. 13, No. 2, 1997, pp. 125–136.

[20]Le Maître, O. P., Knio, O. M., Najm, H. N., and Ghanem, R. G., "A Stochasitc Projection Method for Fluid Flow," *Journal of Computational Physics*, Vol. 173, No. 2, 2001, pp. 481–511.

[21]Xiu, D., and Karniadakis, G. E., "Modeling Uncertainty in Flow Simulations via Generalized Polynomial Chaos," *Journal of Computational Physics*, Vol. 187, No. 1, 2003, pp. 137–168.

[22]Xiu, D., Lucor, D., Su, C.-H., and Karniadakis, G. E., "Stochastic Modeling of Flow-Structure Interactions Using Generalized Polynomial Chaos," *Journal of Fluids Engineering*, Vol. 124, March 2002, pp. 51–58.

[23]Xiu, D., and Karniadakis, G. E., "Modeling Uncertainty in Steady State Diffusion Problems via Generalized Polynomial Chaos," *Computational Methods in Applied Mechanics*, Vol. 191, No. 43, 2002, pp. 4927–4948.

[24]Chorin, A. J., "Guassian Fields and Random Flows," *Journal of Fluid Mechanics*, Vol. 63, No. 1, 1974, pp. 21–32.

[25]Crow, S. C., and Canavan, G. H., "Relationship Between a Wiener-Hermite Expansion and an Energy Cascade," *Journal of Fluid Mechanics*, Vol. 41, 1970, pp. 387–403.

[26]Millman, D. R., King, P. I., and Beran, P. S., "A Stochastic Approach for Predicting Bifurcation of a Pitch and Plunge Airfoil," AIAA Paper 2003-3515, June 2003.

[27]Millman, D. R., King, P. I., and Beran, P. S., "Airfoil Pitch and Plunge Bifurcation Behavior with Fourier Chaos Expansions," *Journal of Aircraft*, Vol. 42, No. 2, 2005, pp. 376–384.

[28]Pettit, C. L., and Beran, P. S., "Polynomial Chaos Expansion Applied to Airfoil Limit Cycle Oscillations," AIAA Paper 2004-1695, April 2004.

[29]Myers, R. H., and Montgomery, D. C., *Response Surface Methodology: Process and Product Optimization Using Designed Experiments*, Wiley, New York, 1995.

[30]Mathelin, L., and Hussaini, M. Y., "A Stochastic Collocation Algorithm for Uncertainty Analysis," NASA/CR-2003-212153, 2003.

[31]Millman, D. R., King, P. I., Maple, R. C., and Beran, P. S., "Predicting Uncertainty Propogation in a Highly Nonlinear System with a Stochastic Projection Method," AIAA Paper 2004-1613, April 2004.

[32]Atkinson, K. E., *An Introduction to Numerical Analysis*, 2nd ed., Wiley, New York, 1989, pp. 197–246.

[33]de Boor, C., *A Practical Guide to Splines*, Springer-Verlag, New York, 2001.

[34]Ghanem, R., and Spanos, P., "A Stochastic Galerkin Expansion for Nonlinear Random Vibration Analysis," *Probabilistic Engineering Mechanics*, Vol. 8, 1993, pp. 255–264.

[35]Morton, S., and Beran, P., "Hopf-Bifurcation Analysis of Airfoil Flutter at Transonic Speeds," *Journal of Aricraft*, Vol. 36, No. 2, 1999, pp. 421–429.

[36]Thomas, J. P., Dowell, E. H., and Hall, K. C., "Nonlinear, Inviscid Aerodynamic Effects on Transonic Divergence, Flutter, and Limit Cycle Oscillation," *AIAA Journal*, Vol. 40, No. 4, 2002, pp. 638–646.

[37]Kousen, K. A., and Bendiksen, O. O., "Nonlinear Aspects of the Transonic Aeroelastic Stability Problem," AIAA Paper 88-2306, April 1988.

[38]Alonso, J., and Jameson, A., "Fully-Implicit Time-Marching Aeroelastic Solutions," AIAA Paper 94-0056, Jan. 1994.

[39]Stivers, L. S. J., "Effects of Subsonic Mach Number on the Forces and Pressure Distributions on Four NACA 64A-Series Airfoil Sections at Angles of Attack as High as 28°," NACA-TN-3162, 1954.

[40]Tannehill, J. C., Anderson, D. A., and Pletcher, R. H., *Computational Fluid Mechanics and Heat Transfer*, 2nd ed., Taylor and Francis, 1997, Chap. 4.

[41]Hoffmann, K. A., and Chiang, S. T., *Computational Fluid Dynamics*, Vol. II, 4th ed., Engineering Education System, Wichita, KS, 2000, Chap. 12.

[42]Krist, S., Bierdon, R., and Rumsey, C., "CFL3D User's Manual," NASA/TM-1998-208444, 1998.

[43]Whitfield, D., and Janus, J., "Three-Dimensional Unsteady Euler Equations Solution Using Flux Vector Splitting," AIAA Paper 84-1552, June 1984.

[44]Bland, S., "AGARD Two Dimensional Aeroelastic Configurations," AGARD Rept. 156, 1979.

[45]Bhatia, K. G., "A Computer Program for Automated Flutter Solution and Matched Point Determination," NASA TM-X-2846, 1973.

[46]Seydel, R., *From Equilibrium to Chaos: Practical Bifurcation and Stability*, Elsevier Science, New York, 1988, Chap. 2.

[47]Duda, R. O., Hart, P. E., and Stork, D. G., *Pattern Classification*, 2nd ed., Wiley, New York, 2001, Chap. 3.